HAL
open science

Tensile and ductile fracture properties of as-printed 316L stainless steel thin walls obtained by directed energy deposition

Pierre Margerit, Daniel Weisz-Patrault, Krishnaswamy Ravi-Chandar, Andrei Constantinescu

To cite this version:

Pierre Margerit, Daniel Weisz-Patrault, Krishnaswamy Ravi-Chandar, Andrei Constantinescu. Tensile and ductile fracture properties of as-printed 316L stainless steel thin walls obtained by directed energy deposition. Additive Manufacturing, 2020, 37, pp.101664. 10.1016/j.addma.2020.101664 . hal-03042512

HAL Id: hal-03042512

https://hal.science/hal-03042512v1

Submitted on 6 Dec 2020

HAL is a multi-disciplinary open access archive for the deposit and dissemination of scientific research documents, whether they are published or not. The documents may come from teaching and research institutions in France or abroad, or from public or private research centers.

L'archive ouverte pluridisciplinaire **HAL**, est destinée au dépôt et à la diffusion de documents scientifiques de niveau recherche, publiés ou non, émanant des établissements d'enseignement et de recherche français ou étrangers, des laboratoires publics ou privés.

Tensile and ductile fracture properties of as-printed 316L stainless steel thin walls obtained by directed energy deposition

Pierre Margerit[a,*], Daniel Weisz-Patrault[a], Krishnaswamy Ravi-Chandar[b], Andrei Constantinescu[a]

[a]*LMS, CNRS, École Polytechnique, Institut Polytechnique de Paris, F-91128 Palaiseau, France*
[b]*Department of Aerospace Engineering & Engineering Mechanics, University of Texas at Austin, Austin, TX, USA*

Abstract

Mechanical properties of as-printed 316L stainless steel thin-walled structures obtained by directed energy deposition are investigated. In-situ tensile and fracture tests are performed on small samples obtained from a additively manufactured square section tube and extracted with three different orientations with respect to the part build direction. Despite a strongly oriented microstructure resulting from the process, as-printed specimens exhibit a reduced anisotropy in comparison with thick or polished samples commonly reported in the literature. Moreover, it is shown using a simple model that the reduced dentified anisotropy can be explained by considering the material thickness variation pattern only, resulting from the layer stacking process. Fracture tests are analyzed using an adapted digital image correlation procedure that evaluates the specimen fracture toughness from experimentally computed J-integrals. Using time reversal, strain fields in regions close to the crack path are identified. Stress fields are then computed from the constitutive behavior identified in tensile tests. A regularization procedure is proposed to enforce the stress equilibrium. Finally, the J-integral is computed using various integration contours in order to validate its path-independance. On this basis, a nearly isotropic fracture toughness is identified. Additional scanning electron microscope observations show that fracture surface features are independent from specimen orientation. This apparent isotropy is explained by the isotropic distribution of lack-of-fusion defects driving crack initiation and propagation.

Keywords: Direct Energy Deposition, Fracture toughness, Digital Image Correlation, In situ SEM experiment

1. Introduction

In the past decade, additive manufacturing of metals has evolved from a rapid prototyping technique to a process suited for the production of fully functional parts [1]. Among the emerging additive manufacturing technologies, the Directed Energy Deposition (DED) [2] is a process suitable for applications ranging from functionally graded parts [3] to structural repair [4]. In particular, the DED technology enables the quick production of complex thin-walled structures.

*Corresponding author: *pierre.margerit@polytechnique.edu*

Additive manufacturing processes opened a set of challenging questions which received a strong interest from the scientific community [5–7]. Understanding the complex interweaving between process parameters (e.g heat source power, scanning path, powder flow), residual stresses [8–13] and mechanical properties [14] is one of the major issues [15]. The chosen printing strategy has consequences at different scales: (i) at the *microscopic* scale, where crystallization is driven by temperature gradients, resulting in epitaxial grains with orientations highly influenced by the heat source path [16]; (ii) at the *mesoscopic* scale, where the layering process as well as the lack-of-fusion defects result in significant thickness variations responsible for stress concentrations [17]; (iii) at the *macroscopic* scale, where residual stresses associated with heating/cooling cycles are responsible for distortion of parts [8, 9, 18].

Among material characteristics affected by the fabrication process, fracture properties are central for engineering applications, certification and safety. A number of works focus on fracture properties of additively manufactured parts [14]. However, most results related to 316L stainless steel material have been established for Selective Laser Melting (SLM) technology. It has been observed that additively manufactured 316L exhibits higher yield stress and ultimate tensile strength than conventionally manufactured 316L, and a lower elongation to failure and fracture toughness [19]. In addition, the influence of layer orientation and surface roughness on the fatigue behavior of SLM parts were addressed in [20, 21]. The ability to manufacture 316L stainless steel parts using the DED additive manufacturing technology have been investigated in a number of recent works [22–28]. However, most of the studies related to the fracture properties of parts resulting from this specific process have focused on polished Ti-6Al-4V specimens. Anisotropic fracture toughness is usually explained by the morphological texture, as cracks propagate through columnar grains or follow columnar grain boundaries depending on specimen orientation [29]. In contrast, as-printed specimens present significant thickness variations across the build direction associated with the layering pattern. Thus, geometrical effects depending on the applied load direction are expected, in particular when considering additively manufactured thin walls, for which the thickness variations count for a significant proportion of the nominal thickness. Moreover, unmelted particles are randomly distributed at the specimen surface, resulting in a large number of stress concentrations responsible for the initiation and propagation of cracks in the structure. Hence the current literature dedicated to polished specimens can be used only for parts receiving post-processing such as surface machining. In addition, the fracture toughness is usually measured using classical compact tension (CT) specimens. For thin-walled structures though, CT specimens cannot be used as they would buckle under the compressive stresses developing in the bending region. Moreover, in these specimens the process zone is relatively confined near the crack tip (i.e pre-crack or notch) if the material exhibits a brittle fracture behavior. In this case, the fracture toughness can be conveniently determined using the process zone confinement assumption, using classical formulas of stress intensity factors based on linear fracture mechanics. However, because of the relatively high ductility of additively manufactured 316L material, a large plastic zone would develop around the crack tip of a notched specimen, requiring a more detailed investigation concerning the validity of the process zone confinement assumption.

The present work is dedicated to the characterization of tensile and fracture properties of as-printed thin-walled 316L structures fabricated by DED. In particular, the objective is to understand to what extent specific microstructures, lack-of-fusion defects (i.e., unmelted particles), and

thickness variations contribute to the overall fracture behavior. In addition, a procedure leading to the evaluation of the the material toughness is proposed, with the aim to overcome problems associated with thin-walled structures made of 316L stainless steel: (i) a low thickness preventing the use of classical CT specimens and (ii) a large plastic zone (ductile fracture process) breaking the assumption of a confined process zone. The analyzed specimens were extracted from a square tube fabricated by laser metal powder directed energy deposition (LMPDED). A close image of the as-printed material showing layers and lack-of-fusion defects is presented in figure 1. Strong crystallographic and morphological textures are also observed. To identify a potential anisotropy of the mechanical behavior, specimens have been extracted along three different orientations, namely: the build direction (verical Z-axis), the print direction (horizontal X or Y-axis) and the oblique direction (i.e., 45°).

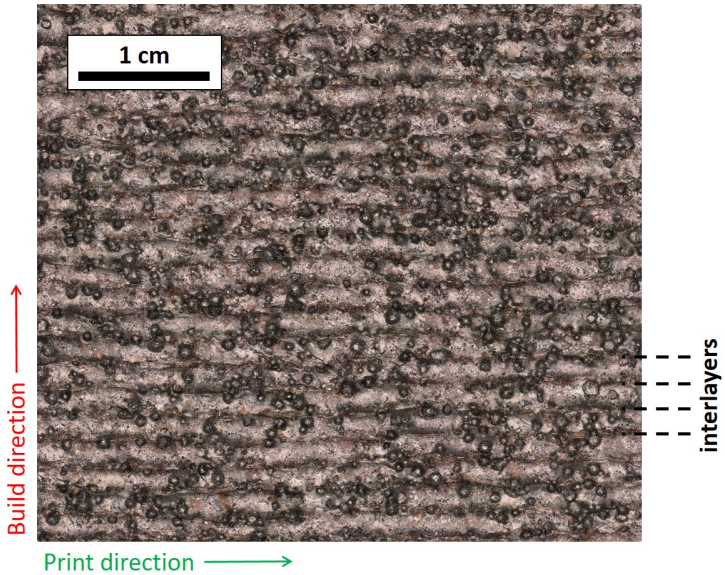

Figure 1: Close image of the as-build material surface showing the printing layers and the unmelted particles. Interlayers are separated of a distance of 200μm.

The proposed procedure starts with the identification of the elastic-plastic material constitutive behavior determined by tensile tests on dog-bone specimens. The identified material parameters are observed to be slightly dependent on the specimen orientation. A simple model is introduced to estimate the influence of the thickness variation pattern. Based on an analogy with springs and sliding frictional elements (disposed in parallel or series according the specimen orientation), it shows that the apparent anisotropy identified may be largely explained by the thickness profile instead of the textured microstructure.

Once the material constitutive behavior is known, it is proposed to determine the material fracture properties from the mechanical fields in the neighborhood of the crack tip of a single-edge notched specimen. More precisely, displacement fields are measured by digital image correlation (DIC) techniques [30, 31]. The main difficulty in assessing fracture properties from displacements obtained by DIC arises during crack propagation where neighboring pixels get separated. Thus the identification process of local fields becomes unstable and significant errors can occur. To overcome

this difficulty, a backward DIC scheme is preferred. It consists of defining the final loading stage as the reference image, and performing the correlation gradually from the final image to the first one. This original procedure evaluates strains close to the crack surfaces. Since the anisotropic elastic-plastic behavior has been previously identified on dog-bone specimens, a simple algorithm is proposed to estimate elastic and plastic strains and stresses (with elastic trial and plastic correction by a radial projection scheme). However, due to measurement uncertainties, this procedure leads to stresses not satisfying equilibrium. Thus, the procedure includes a correction based on a minimization between the initial stress field estimation (i.e., not verifying the equilibrium) and the corrected stress field, under the constraint of stress equilibrium. This constrained minimization is performed within the framework of Lagrange multipliers, leading to a diffusion equation that has to be solved at each time step to obtain the corrected stress field.

Since the distribution of the strains and stresses has been determined, the evolution of the process zone can be followed during each step of the test (stress concentration buildup, crack initiation and propagation). In addition, the classical path-independent J-integral [32] is computed from the identified mechanical fields. The results show that this experimental J-integral is path-independent up to the crack initiation where it equals the critical energy release rate and is equivalent to the fracture toughness [32]. The obtained critical energy release rate values are similar for the three tested directions. In addition, no kinked cracks are observed in all experiments. This is likely due to the effect of unmelted particles that are responsible for stress concentration and void nucleation guiding the crack path. Since these defects are isotropically distributed at the specimen surface, the crack path and fracture toughness are more or less isotropic.

To support this hypothesis, the study is complemented by in-situ Scanning Electron Microscope (SEM) observations to understand in more detail the fracture mechanisms. Interestingly, stress concentrations as well as void nucleations detected near the unmelted particles are observed to drive the crack propagation path, confirming their role in the fracture behavior.

The paper is organized as follows. The section 2 details aspects related to the manufactured material: specimen fabrication, geometrical analysis and microstructure analysis. In section 3 the experimental setup is presented as well as numerical methods: DIC, stress computation and correction, J-integral evaluation. Sections 4 and 5, respectively, present the tensile tests on dog-bone specimens and fracture tests on notched specimens. Finally, complementary in-situ SEM experiments are presented in section 6.2. Conclusive remarks are given in section 7.

2. Materials

2.1. Specimen fabrication

The specimens analyzed in the present work were fabricated by LMPDED with a BeAM™ machine. The powder used in this study is MetcoClad™ 316L-SI, whose chemical composition is provided in table 1. In general, the mechanical properties of additively manufactured material are highly dependent on process parameters (e.g., laser power, powder feed rate, laser path and velocity). However, a consistent experimental characterization relies on homogeneous material properties. As a consequence, the part from which the specimens are extracted has to be designed so that the laser power and velocity and the powder feedrate are kept as steady as possible during the process. The ideal candidate structure is, therefore, a circular cylinder created following a

helical path, thus resulting in constant process parameters. In order to obtain flat specimens, it has been chosen here to fabricate cylinders with a square section (see Fig. 2). The cylinder was manufactured on the substrate and later removed using an electric saw. It should be noted that specific supports could have been designed to easily deal with the removal task [33]. The samples were finally extracted out of the flat faces by water-jet cutting. Process parameters chosen for this study are listed in table 2.

An important feature is the development of residual stresses in the manufactured part due to the high thermal gradients involved in the process. This eventually leads to large distortions. In the present case, these distortions are associated with the wavy pattern that can be observed in the manufactured tube (see figure 2). In order to reduce the magnitude of these distortions as much as possible, the size of the tube section was kept relatively small, thus reducing the length of the specimens that could be extracted. At the end of the process, residual stresses are almost completely released during the specimen cut (e.g., residual stresses magnitude is estimated to 100 MPa in [16]), and almost flat specimens are obtained.

With the aim to quantify the anisotropy in the material constitutive properties, specimens have been extracted according to three different orientations, namely: $0°$, $45°$, and $90°$ corresponding respectively to the build (red), oblique (blue) and print (green) directions in figure 2. Two different types of specimens have been extracted namely: dog-bone specimens and notched specimens, respectively dedicated to tensile tests and fracture tests. The notch diameter (1.5 mm) is limited by the water beam diameter.

Table 1: Chemical composition in weight percent

Fe	Ni	Cr	Mo	Si	Mn	C	Others
Balance	12	17	2.5	2.3	1	0.03	$\leq$0.5

Table 2: Process parameters for the tube

Laser velocity	(mm.s^{-1})	33
Laser power	(W)	245
Laser beam radius	(mm)	0.338
Dwell time	(s)	0
Layer spacing (Z-axis step)	(mm)	0.2
Powder flow rate	(g.s^{-1})	6

2.2. *Surface roughness*

The surface roughness resulting from the fabrication process was characterized using surface elevation measurements performed with a Keyence™ VHX-6000 optical microscope equipped with a 250× magnification lens. The total apparent thickness, measured with a caliper, is approximately $H = 800$ µm. However, lack-of-fusion defects are distributed on the surface, as show in the figure 1. These spheres have a diameter similar to the powder, (i.e., $D = 65$ µm on average). As already mentioned, these spheres favor local stress concentration, but do not contribute significantly to the

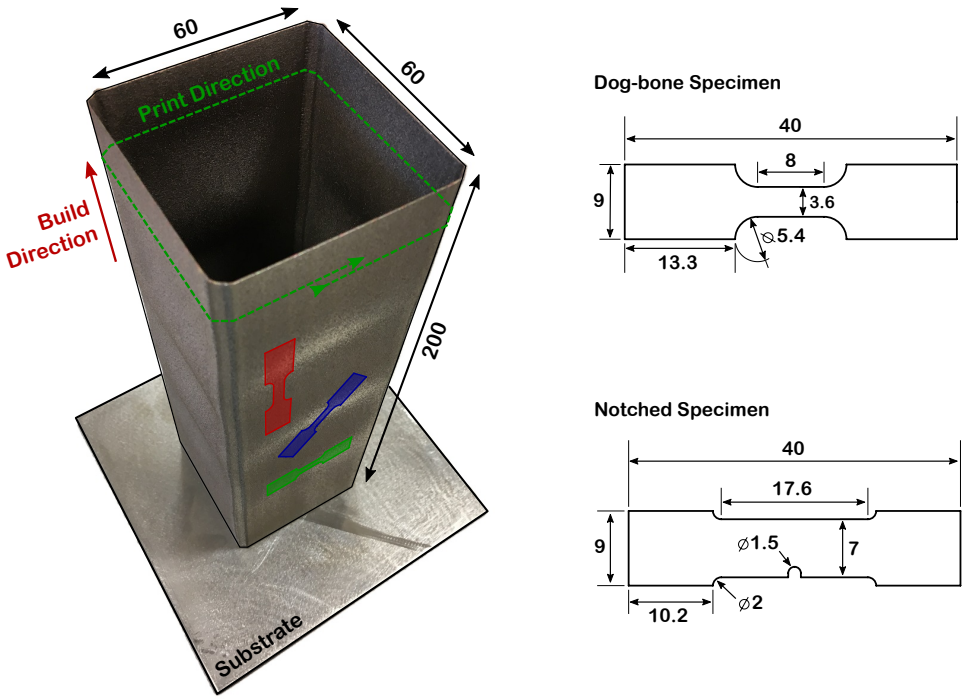

Figure 2: Geometrical definition of the 316L stainless steel tube and the extracted specimens showing the different orientations: build direction (red), print direction (green) and oblique (45°, in blue). All lengths are in mm.

overall elastic-plastic behavior. Thus the *effective* thickness across the build direction, denoted by $h(z)$, should exclude the additional thickness due to lack-of-fusion defects. In addition, a pattern associated with the layering process can be distinguished under the unmelted particles. Indeed, the cross section along the build direction presents a period $\Delta z = 200$ µm, corresponding to the layer spacing (see table 2). The detailed thickness variation for each period is closely related to the melt pool shape, and its amplitude estimated was estimated to around $\Delta h = 200$ µm by crude peak-to-peak measurements. Thus, the effective thickness $h(z)$ across the build direction can be roughly interpolated by the following function:

$$h(z) = h_0 + \Delta h \left| \sin\left(\frac{\pi}{\Delta z} z\right) \right| \tag{1}$$

Where $h_0 = H - 2D - \Delta h = 470$ µm. The interpolated cross section along the build direction is presented in figure 3, and the average effective thickness is around $h_N = 600$ µm and is used as the nominal thickness for tensile tests.

2.3. Microstructural analysis

The microstructural analysis explores the grain morphology and the underlying crystallographic texture resulting from the additive manufacturing process. Specimens were prepared by surface polishing with subsequent sand papers (400 to 4000) followed by a 1 µm grinding powder. Specimens were finally ion polished during one hour with the following parameters: 6° polishing

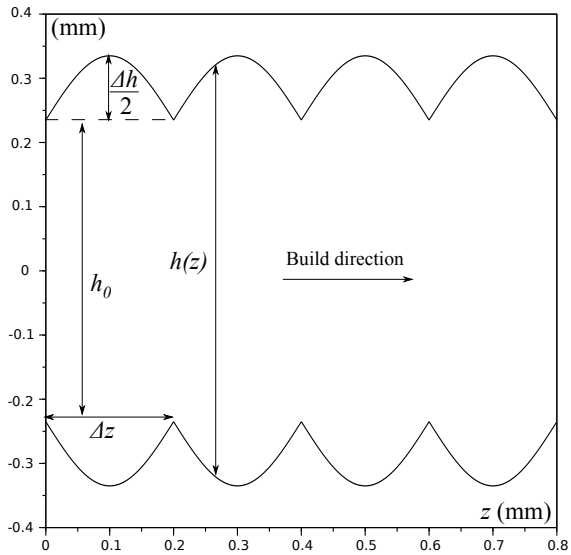

Figure 3: Idealized cross section pattern along the build direction.

angle, 6 keV electron beam power and 6 rpm specimen angular velocity in a PECS II machine from Gatan™. The microstructural characterization is carried out using a SEM equipped with a 3000 Hz electron back-scatter diffraction (EBSD) camera with a 0.350 µm sampling step and a 1200×1800 µm observation zone.

The pole figures are presented in figures 4 (a) and (b). No preferred crystal orientation can be identified, even though a higher density can be distinguished with a 4-fold decrease in the $\{100\}$ pole figure, corresponding to face cubic center (FCC) faces orientated along the build direction. Grain morphology is characterized on the EBSD map presented in figure 4 (b), where the interfaces between layers are indicated by dotted lines. The microstructure is mostly composed of long epitaxial grains, in agreement with previous results in the literature [23, 25, 26]. Small grains are defined by an area A verifying $A < 80$ µm^2, which corresponds to an equivalent diameter $D_{\text{eq}} \approx 10$ µm. The fraction of small grains is computed as a function of height (build direction), and presented in figure 4(c). In the neighborhood of the inter-layer regions a higher fraction of small grains (with a ratio of 2 to 1) is observed, in agreement with [16]. The distribution of the grain orientations, defined as the angle between the equivalent ellipse major axis and the print direction, is presented in figure 4(d). The grains exhibit a preferred orientation of 71°, related to the direction of the temperature gradient in the process, which depends on the laser scanning direction (from left to right) [16, 28]. In addition, the distribution of grain aspect ratios and grain areas are presented in figure 4(e) which shows that smaller grains tend to be spherical, while the aspect ratio increases with the grain area.

3. Methods

The complete procedure for the identification of the fracture toughness is divided into: (i) the experimental setup, (ii) the identification of strains by DIC, (iii) the computation of stresses, and (iv) the evaluation of J-integrals. The following paragraphs focus on the presentation of the method.

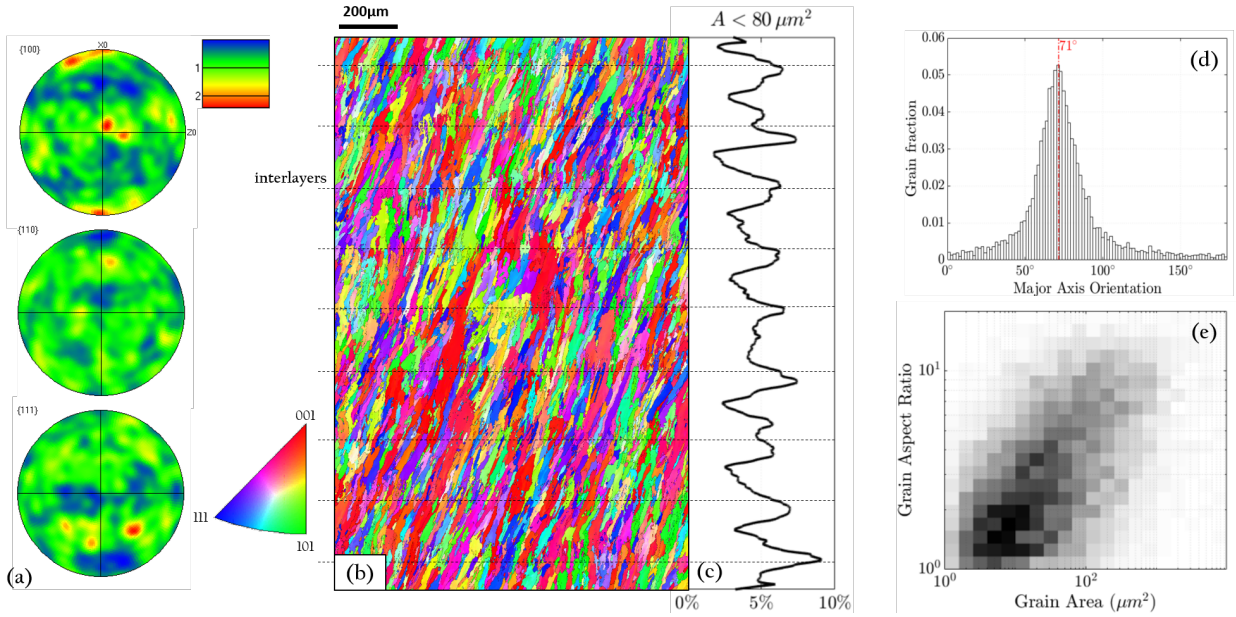

Figure 4: Microstructure analysis. (a) Pole figures; (b) EBSD Map (IPF-X); (c) Small grain area fraction; (d) Orientation of the major axis of the equivalent elliptical grain; (e) Grain aspect ratio distribution vs. grain area distribution.

The experimental results are presented in the sections 4 and5.

3.1. Experimental setup for in-situ mechanical testing

The experimental tests are performed *in-situ* under a Keyence™ VHX-6000 optical microscope equipped with a 50× magnification lens. The load is applied monotonically up to failure with a small-scale tensile machine (MTI™ SEMTester-1000).

The experimental characterization is complemented in section 6.2 by in-situ SEM observations. A notched specimen is monotonically loaded up to failure with the same small-scale tensile machine. A 100× magnification is used, with a beam tension of 10kV at a working distance of 32mm, resulting in an observation zone of approximately 1mm^2.

3.2. Global digital image correlation

In the present work, the *global* formulation of the digital image correlation method is used [30]. Given a *reference* image f and a *current* image g, the DIC procedure consists of solving the following minimization problem:

$$\boldsymbol{u} = \min_{\boldsymbol{u}^*} \int_{\Omega} \Big(f(\boldsymbol{x}) - g\big(\boldsymbol{x} + \boldsymbol{u}^*(\boldsymbol{x})\big)\Big)^2 \, \mathrm{d}\Omega \tag{2}$$

where $\boldsymbol{x}$ is the position, $\boldsymbol{u}$ is the transformation from f to g and Ω the correlation domain. The classical *local* implementation of DIC solves this problem on a number of small sub-domains Ω with rather simple displacement functions $\boldsymbol{u}(\boldsymbol{x})$. Alternatively, the *global* DIC procedures uses

a finite-element-like formulation, discretizing the transformation function $\boldsymbol{u}$ by means of a mesh covering the entire Region Of Interest (ROI):

$$\boldsymbol{u}(\boldsymbol{x}) = \boldsymbol{N}(\boldsymbol{x}) \cdot [\boldsymbol{u}] \tag{3}$$

where the unknown $[\boldsymbol{u}]$ correspond to the nodal displacements and the interpolation matrix $\boldsymbol{N}(\boldsymbol{x})$ contains the finite element (FE) shape functions. Such a formulation presents several advantages. First, strains are computed as in usual FE schemes (by derivation of $\boldsymbol{N}(\boldsymbol{x})$), which avoids smoothing issues and finite difference schemes as in local DIC [34]. Second, the FE mesh accurately follows the object geometry, allowing the identification of displacements at the edges (e.g crack surface, see section 3.3) without being influenced by the image background.

Solving the non-linear problem (2) requires the implementation of an iterative Newton-Raphson procedure (see [35] for more details). In this work, the minimization problem is solved in Matlab™ [36]. Meshes with linear triangular elements are defined using the unstructured DistMesh generator by Persson [37]. At the end of the procedure, a set of configurations is obtained, represented by the set of nodal positions $[\boldsymbol{x}]_i$ (with $i = 1, \ldots, N$ the image index). Considering the transformation gradient $\boldsymbol{F} = \partial\boldsymbol{x}/\partial\boldsymbol{X}$ with respect to the initial configuration $\boldsymbol{X} = \boldsymbol{x}_1$, the strain rate $\dot{\varepsilon}$ and total strain ε can be computed. Since linear elements have been chosen, these fields are piece-wise constant.

3.3. Crack opening and backward-DIC scheme

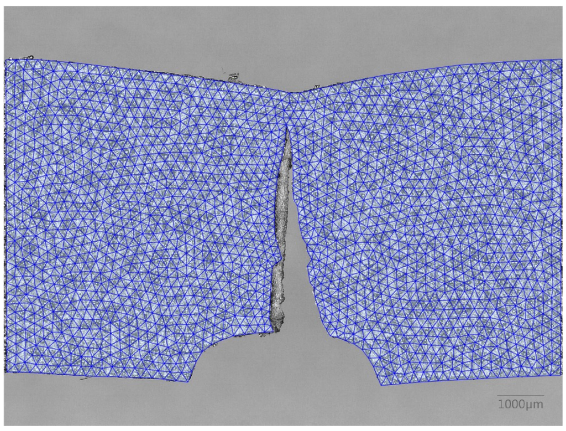

Figure 5: DIC mesh defined at the initial loading stage.

For the fracture tests, the crack opening poses several difficulties for DIC when the reference image is defined at the initial step (pristine specimen), as the separation of pixels during the crack propagation introduces artifacts in the correlation procedure. Classical approaches adapt the correlation domain at each time step by erasing elements with the local correlation coefficient as selection criterion [31]. However, the deletion threshold is often difficult to tune and the success of the procedure is not guaranteed. In order to overcome this difficulty, the procedure proposed here starts at the *final* loading stage, just before specimen failure (see figure 5). At this specific stage, the crack geometry is well defined (see figure 5), and the DIC can be performed in the *backward*

direction, from the final stage to the initial stage. Thus, the DIC domain remains unchanged during this procedure. Finally, displacements and strains are computed with respect to the *initial* configuration (i.e., $\boldsymbol{X} = \boldsymbol{x}_1$) as for classical approaches.

3.4. Stress field estimation

The experimental evaluation of the J-integrals requires that both strain and stress fields are known on the contour path. However, at this stage, only the kinematic fields have been computed from the DIC procedure, as well as the measured resultant force F at the specimen boundaries. Ideally, the stress field should derive from the constitutive law applied to the identified strain field, and should be statically admissible, such that both momentum equations (quasi-static regime without body forces) and boundary conditions are fulfilled:

$$\mathbf{div}\,(\boldsymbol{\sigma}) = 0 \qquad \boldsymbol{x} \in \Omega \tag{4}$$

$$\boldsymbol{\sigma} \cdot \boldsymbol{n} = \boldsymbol{T} \qquad \boldsymbol{x} \in \partial\Omega \tag{5}$$

where Ω and $\partial\Omega$, respectively, denote the domain and its boundary on the current configuration, $\boldsymbol{\sigma}$ the tensor field of stress, $\boldsymbol{n}$ the unit outward normal on boundaries, and $\boldsymbol{T}$ is the applied surface traction. Experimentally, the boundary is partitioned between free surfaces where $\boldsymbol{T}$ vanishes and loaded surfaces for which only the resultant traction F is known:

$$F = \boldsymbol{e}_m \cdot \int_{\partial\Omega_F} \boldsymbol{T}\ \mathrm{d}S \tag{6}$$

where $\boldsymbol{e}_m$ denotes the direction of the applied tension.

Recently, it has been proposed that the stress field be evaluated without *a priori* information on the constitutive law [38]. However, this so-called *data-driven* approach is limited to the non-linear elastic case [39], which is not suitable for the present contribution. Instead, the stress identification procedure is divided into two steps. First, an initial estimation of the stress field is computed by applying a constitutive law on the experimental strain field. Due to measurement uncertainties, the obtained stress field is unbalanced. Second, a corrected stress field is computed as the closest candidate stress field satisfying the momentum equations (4).

The first step necessitates the identification of an elastic-plastic constitutive behavior. For the present work, a Von Mises material with a non-linear isotropic hardening law is considered (kinematic hardening being neglected) and identified with tensile tests on dog-bone specimens (see section 4). Thus, the first estimation simply relies on a classical algorithm with elastic trial and plastic correction by a radial projection scheme and estimates elastic and plastic strains and stresses as detailed in Appendix A. However, as the DIC procedure is only able to identify the in-plane strain components of the specimen top surface, additional assumptions on the out-of-plane direction are required. Since specimens are relatively thin, stresses are computed under plane stress assumption. Moreover, assuming large plastic deformations, volume variations are negligible, leading to a purely deviatoric strain tensor.

The second step is a constrained minimization procedure and is detailed in Appendix B. At each time step, an auxiliary boundary value problem is solved, defined on the FE mesh already introduced for the DIC. An illustration is shown in figure 6, with (a) the initial equivalent stress

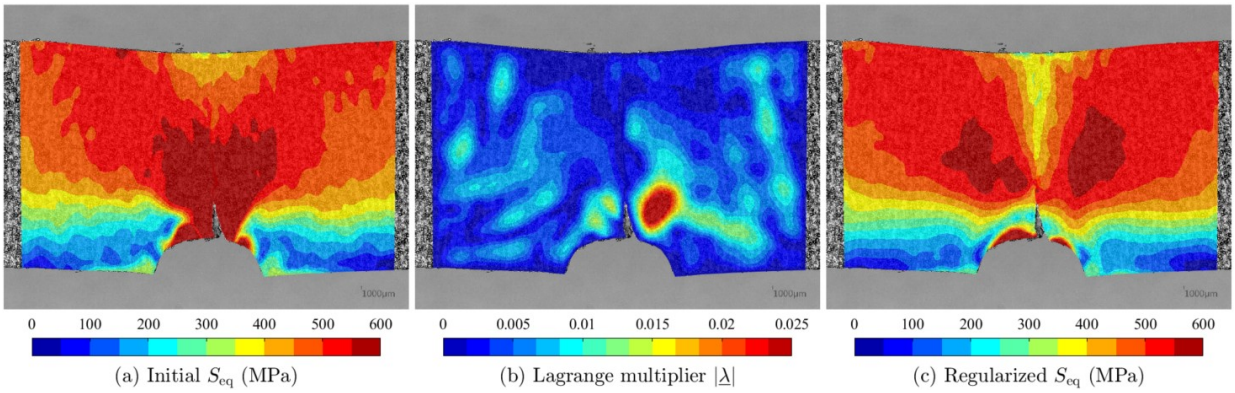

(a) Initial S_{eq} (MPa) (b) Lagrange multiplier $|\underline{\lambda}|$ (c) Regularized S_{eq} (MPa)

Figure 6: Stress regularization by equilibrium enforcement: (a) initial equivalent stress field; (b) Lagrange multiplier field associated with the constraint; (c) regularized equivalent stress field. A relaxed stress zone in front of the crack reveals the classical butterfly distribution around the crack tip.

field, (b) the norm of the resulting Lagrange multiplier field, and (c) the corrected equivalent stress. Constraining the equilibrium (4) has a smoothing effect on the stress field, which is an asset in the elastic regime with a low signal-to-noise ratio due to small strains.

3.5. Path independent J-integral

The proposed approach coupling DIC and stress correction (see sections 3.2 and 3.4) permits the direct observation of the evolution of the process zone, from which the classical path-independent J-integral can be computed [32]. For any contour Γ enclosing the crack tip, the following J-integral denoted by $\mathcal{J}$ reads:

$$\mathcal{J} = \int_{\Gamma} \left[\Psi \, \boldsymbol{n} - \boldsymbol{T} \cdot \frac{\partial \boldsymbol{u}}{\partial \boldsymbol{x}} \right] \cdot \boldsymbol{e}_d \, \mathrm{d}\Gamma \tag{7}$$

where $\boldsymbol{e}_d$ is the crack propagation direction, $\boldsymbol{n}$ the normal to the contour, $\boldsymbol{T} = \boldsymbol{\sigma} \cdot \boldsymbol{n}$ the traction vector, $\boldsymbol{u}$ the displacement, and Ψ the stress work density defined as:

$$\Psi = \int_t \boldsymbol{\sigma} : \mathrm{d}\boldsymbol{\varepsilon} \tag{8}$$

The J-integral is path-independent provided that the integration contours Γ fully contain the dissipation zone (e.g. plasticity, damage).

4. Tensile tests

Monotonic tensile tests performed on dog-bone specimens were performed to: (i) estimate the apparent anisotropy, and (ii) identify an equivalent elastic-plastic constitutive law needed for stress computation (see section 3.4). The experimental setup is presented in section 3.1. Specimens of each orientation (build, oblique and print directions) are monotonically loaded up to failure with a 0.1 mm.min^{-1} extension rate, corresponding to approximately $2 \cdot 10^{-4}\mathrm{s}^{-1}$ strain rate. The interval between two optical microscope image acquisitions is fixed to 15 s, which corresponds to a 0.3% strain step, sufficiently small to capture the elastic regime.

The DIC procedure is applied on a *virtual gauge* defined on the reference image. It is located on a region where the strain distribution is relatively homogeneous (with less than 10% variation with respect to the mean), far from the region of strain localization or failure. The domains corresponding to the virtual gauges are presented in figure 7 for all specimens. The chosen gauge position and size depend on the specimen, as the failure occurred at different locations. Therefore, the measured stress-strain behavior is not affected by strain localization and thus the elastic unloading of the material with the crack propagation captured.

The true stress-true strain curves are presented in figure 7. The stress was computed from the applied load using the nominal thickness fixed to $h_N = 600$ µm as detailed in section 2.2. For each test, a simple uni-axial elastoplastic constitutive law is identified, with isotropic non-linear hardening of the form:

$$\sigma_{\mathrm{y}}(p) = \sigma_{\mathrm{y}}^0 + K p^n \tag{9}$$

where $\sigma_{\mathrm{y}}(p)$ denotes the true yield stress, σ_{y}^0 the initial yield stress, p the cumulative plastic strain, K the hardening modulus, and n a power-law coefficient. The Young moduli E and E' were identified, respectively, from the loading and unloading phases. This characterizes the occurrence of damage, if $E' < E$. The identified material parameters are listed in table 3. The results are in agreement

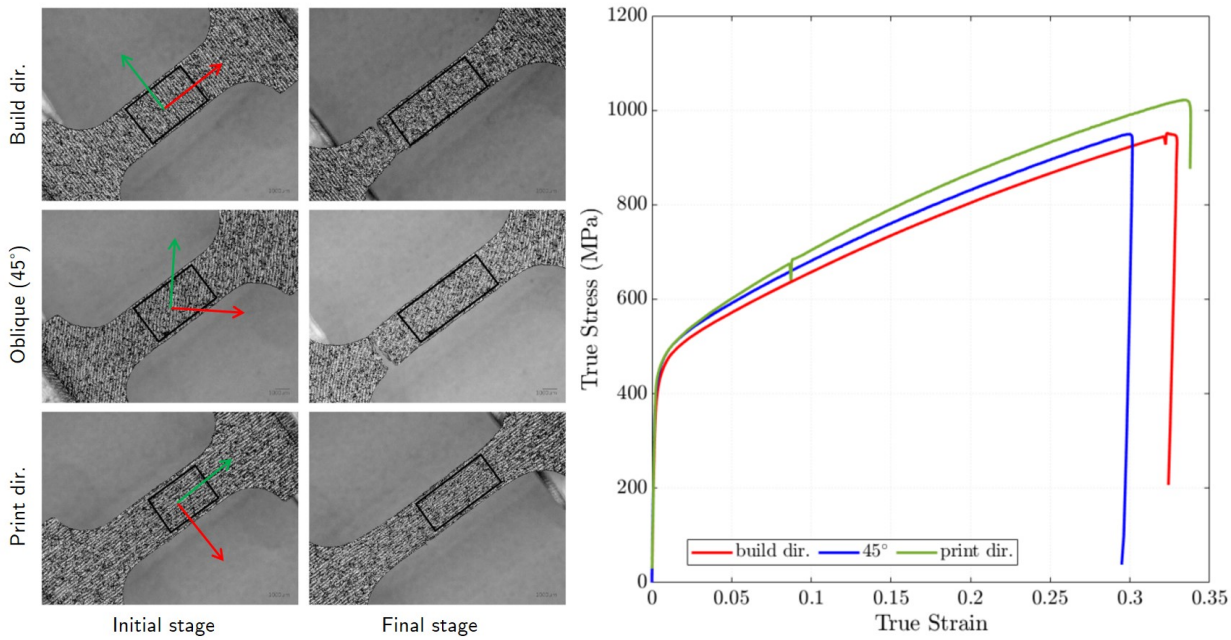

Figure 7: Tensile tests. Left: optical microscope images at the initial and final stages and for the three considered orientations; the virtual gauges used to measure the strains are denoted by black rectangles. Right: resulting true stress - true strain curves.

with isotropic tensile properties of bulk 316L specimens reported in the literature [23, 26]. The variation of material parameters is small: 2%, 5% and 6%, respectively, for Young modulus E, yield stress σ_y and hardening modulus K. This apparent anisotropy may be the consequence of: (i) the oriented microstructure morphology; (ii) residual stresses developing during the manufacturing

	E (GPa)	ν	σ_y^0 (MPa)	K (MPa)	n	E' (GPa)	$\mathcal{J}_C$ (kJ/m^2)
Build dir.	197	0.47	419	1136	0.67	137	702
Oblique (45°)	201	0.40	441	1177	0.68	151	785
Print dir.	201	0.35	431	1203	0.63	195	644

Table 3: Tensile tests. Identified material parameters associated with an equivalent elastic-plastic material with a non-linear hardening law $\sigma_y(p) = \sigma_y^0 + K\,p^n$.

process; (iii) the wall thickness variation pattern. While investigating the effects of the two first causes would required further experiments, the consequence of thickness variations can be studied easily. To this aim, a model based on an analogy with springs and sliding frictional elements is detailed in Appendix C. These elements are, respectively, disposed in parallel and in series for the print and build directions. Assuming a unique elastic-plastic behavior for both print and build directions, one can roughly reproduce the overall anisotropic behavior observed in figure 7.

Furthermore, optical microscope images at the final loading stage are presented in figure 8. Images contain both pristine regions (at the left of specimens with a larger width) and highly deformed regions near the maximum strain localization, so that one can qualitatively estimate the effect of deformation on the thickness profile. Figure 8 shows a clear geometrical effect. As the thickness profile is significantly flattened for the build direction, it is not significantly affected for the print direction and undergoes an intermediate flattening for the oblique direction.

5. Fracture tests

The fracture tests are performed on single-edge-notched tension specimens with three material orientations.

5.1. Measurements

The results of the experiments are represented in the figure 9, where the applied load is plotted as a function of the mean engineering strain for each specimen. In addition, the crack initiation is denoted with a circled marker and corresponds to the peak load. In the later stages, the load monotonically decreases with the crack propagation, which implies that the crack is stable under displacement control only. Several loading stages are highlighted with dot markers: the corresponding equivalent strain maps for the build direction specimen are represented on the top-left side of figure 9(a-f). These strain fields have been identified using the backward-DIC scheme described in section 3.3. Before the crack initiation (from (a) to (c)), strains present a classical butterfly-shaped distribution. As the crack starts to propagate, strains concentrate near the crack flanks. It was observed that the different specimen orientations exhibit comparable load/strain curves and strain maps. This can be seen in the bottom of the figure 9, where the strain maps corresponding to the the crack initiation are represented for each specimen.

5.2. Fracture toughness estimation

The critical energy release rate $\mathcal{J}_C$ is a crack propagation criterion connected to the path-independent J-integral [32]. It is determined by computing the J-integral as a function of the

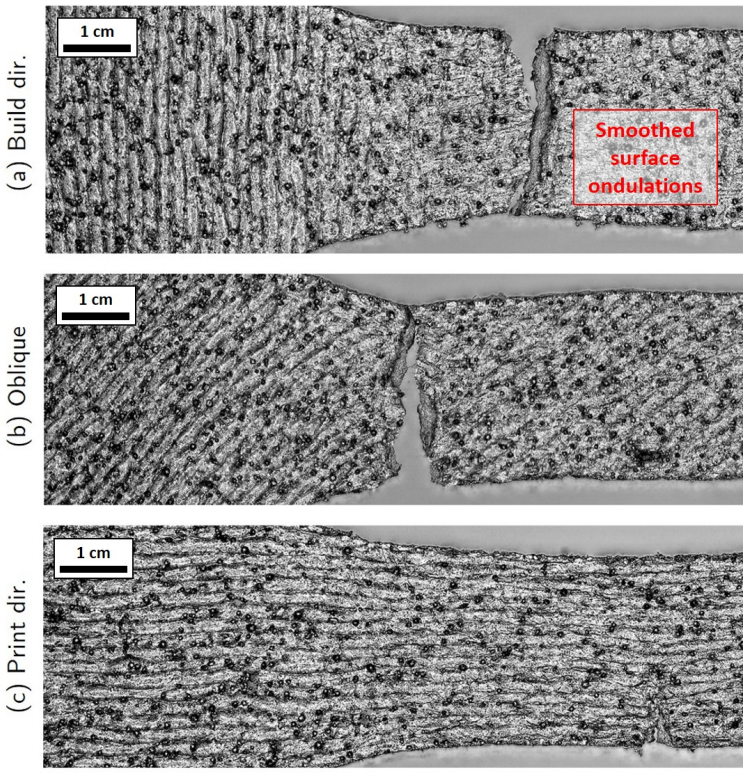

Figure 8: Tensile tests. Optical microscope images of the specimen surface at the final loading stage, for the different specimen orientation.

loading stages and selecting the value reached by $\mathcal{J}$ when the crack starts to propagate. In figure 10b it is shown that the J-integral is rigorously path-independent before crack nucleation as the specimen undergoes monotonic plastic deformation, which is similar to non-linear elasticity. However, when the crack propagates, elastic unloading arises near the crack flanks due to the free traction condition. Since plastic strains spread on a relatively large area, several contours have been tested (see figure 10a) to determine whether the J-integral is path-independent for sufficiently large contours (enclosing the process zone). Very similar J-integrals are obtained for contours (c) and (d) in figure 10b, which indicates that all the dissipation has been taken into account.

The J-integrals computed using the largest contour and applied to all fracture tests are presented in figure 11. For each specimen orientation, the stress field have been computed using the constitutive material behavior identified from the corresponding tensile test (see the section 4), thus sampling the slight anisotropy in the material properties. It can be noticed that similar $\mathcal{J}$ curves are obtained for all specimen directions. In particular, the critical energy release rates $\mathcal{J}_C$, indicated with dot markers and reported in table 3, show a variation of 20% with respect to the mean value $\mathcal{J}_C = 710kJ/m^2$. The reduced difference between specimen orientations is more likely due to random defects than systematic anisotropy. Moreover, the similarity between the identified critical energy release rate demonstrate the repeatability of the proposed procedure. As a consequence, the mean of the critical energy release rates of all specimen orientations can be considered as an isotropic toughness value. As a perspective of work, this averaging could be supported by a

statistical analysis based on multiple test realizations for each specimen orientation. The identified mean critical energy release rate is higher than values of approximately $\mathcal{J}_C = 200kJ/m^2$ reported in the literature concerning steel sheets [40, 41] identified on thicker samples ($h \approx 1.5$ mm). However, it is well-known that the $\mathcal{J}_C$ is highly dependent on the material thickness, and the

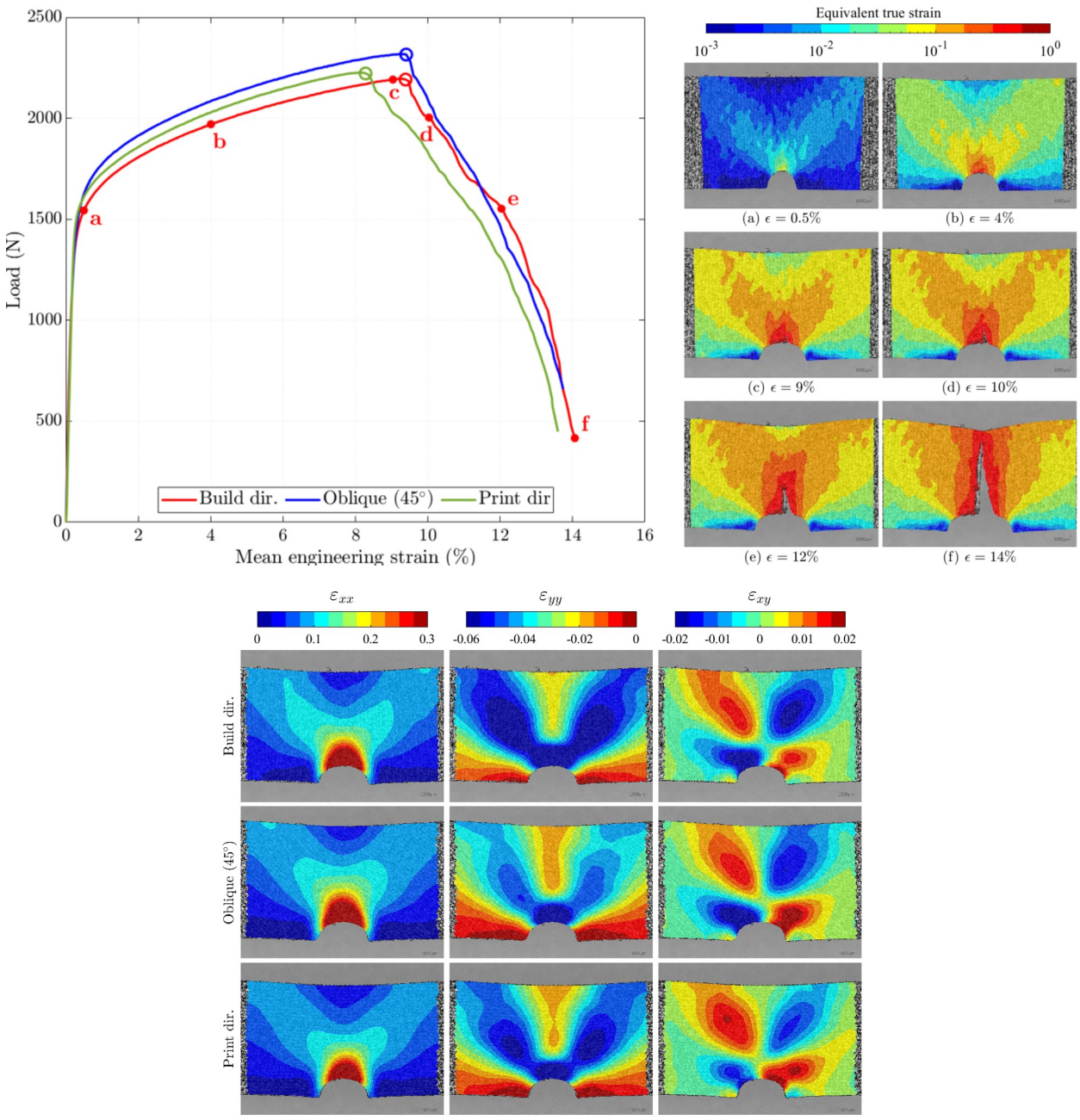

Figure 9: Fracture tests. Top left: measured load versus engineering strain showing elastic, plastic and unloading regimes; the crack onset is denoted by a circled marker. Top right: equivalent true strain maps for the build direction specimen, taken at different loading stages. Bottom: Strain maps just before crack onset corresponding to each specimen orientation obtained using classical forward DIC.

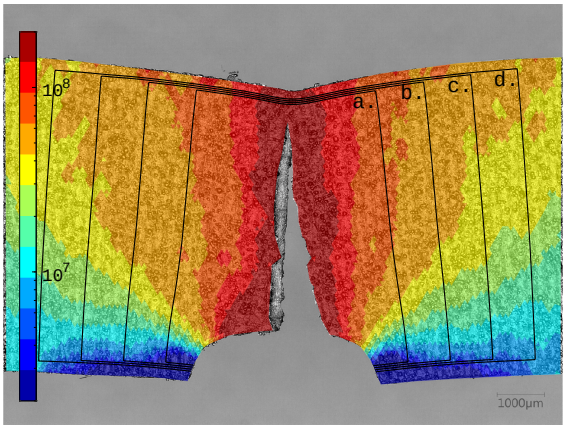

(a) Spatial distribution of the mechanical stress work Ψ (see Eq. (8)) and integration paths in the final configuration.

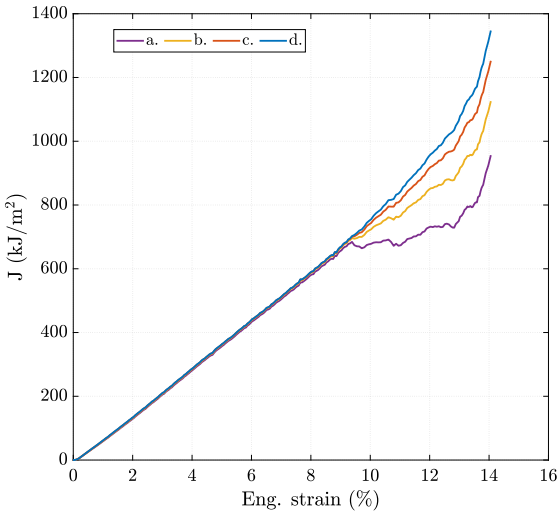

(b) Evolution of the J-integral values corresponding to the contour paths as a function of the engineering strain.

Figure 10: Evaluation of the J-integral using different contour path applied to the results of the build direction specimen.

values reported here are in agreement with the 3-fold increase of $\mathcal{J}_C$ that have been observed at the sub-millimeter range in [42, 43].

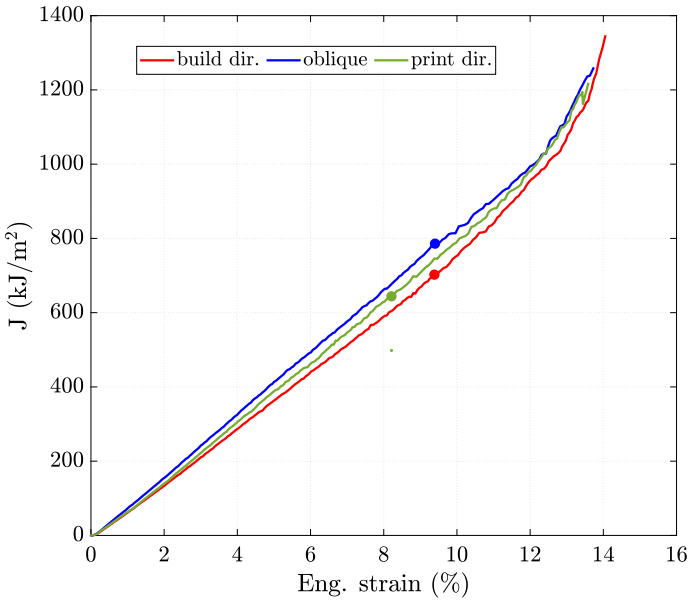

Figure 11: J-values associated with each specimen orientation, computed with the contour (d) in figure 10b. Dot markers denote the critical value J_c corresponding to the crack onset.

6. In-situ SEM observations

This section presents complementary SEM observations. First, the crack surfaces resulting from the fracture tests are analyzed. Second, an additional fracture test is performed in-situ, with

an observation zone focusing at the notch vicinity.

6.1. Crack surface characterization

Crack surfaces are presented in figure 12. On the left panel, a view of the print orientation specimen is presented, showing the crack surface and the wavy thickness pattern with the interlayers. Unmelted spherical particles can also be seen, revealing their poor cohesion with the bulk. Therefore, these lack-of-fusion defects act as stress concentrators and void nucleation sites, driving the crack initiation and propagation. A closer view of the crack surface of the build direction specimen is presented on the right panel of the figure 12. Dimple structures can be observed, characteristic of a ductile fracture process. Thus, large plastic deformations in the bulk are driving the overall fracture behavior.

A quantitative analysis of the dimple structure size distribution is presented in figure 13 for the build and oblique directions. The equivalent diameter of dimples is computed through image segmentation (see Appendix D for details). Similar distributions are obtained, which strengthens the hypothesis that fracture mechanisms are more or less isotropic.

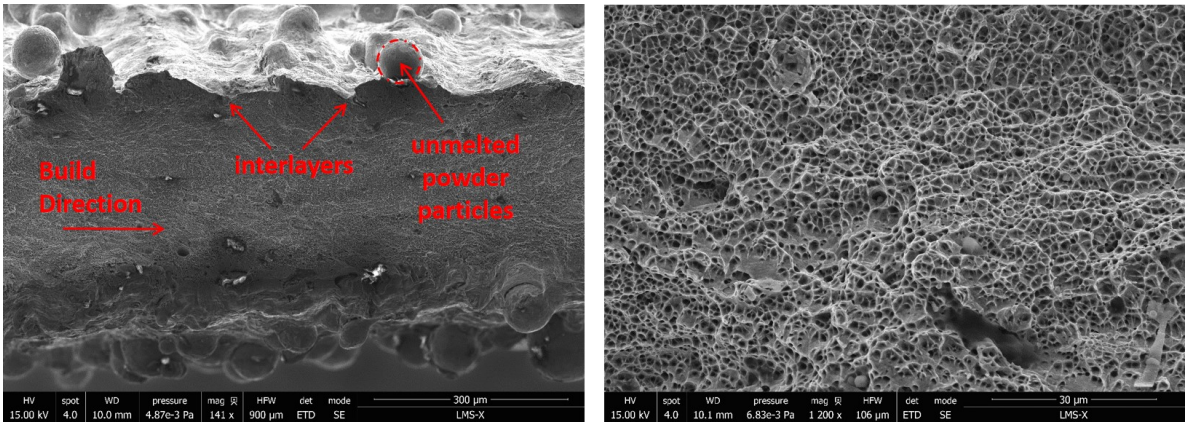

Figure 12: SEM micrographs of crack surfaces. Left: global view (print direction specimen); right: close view of dimple structures (build direction specimen).

6.2. In-situ SEM fracture test

In order to characterize the effect of surface roughness of the crack initiation and propagation, an additional in-situ SEM fracture test was performed on a build direction specimen using the experimental setup detailed in section 3. The load-extension curve is shown in figure 14 (a). Four images were recorded during the test and are labeled (a) to (d). A slight unloading of the setup is observed at each recorded stage, corresponding to the arrest of the loading during the electron beam scanning. The global DIC procedure detailed in section 3.2 is applied to measure the strain field. The equivalent strain map normalized by the mean strain is presented in figure 14 (b) in the early plastic regime (i.e., image (b)). Clear strain localization is observed at inter-layers and regularly spaced of $\Delta_z = 200$ µm. Since smaller grains are located in the inter-layers, lower yield stress is expected in these regions by Hall-Petch effect [44], which could participate in strain localization. While strain localization at inter-layers has been reported on polished specimens

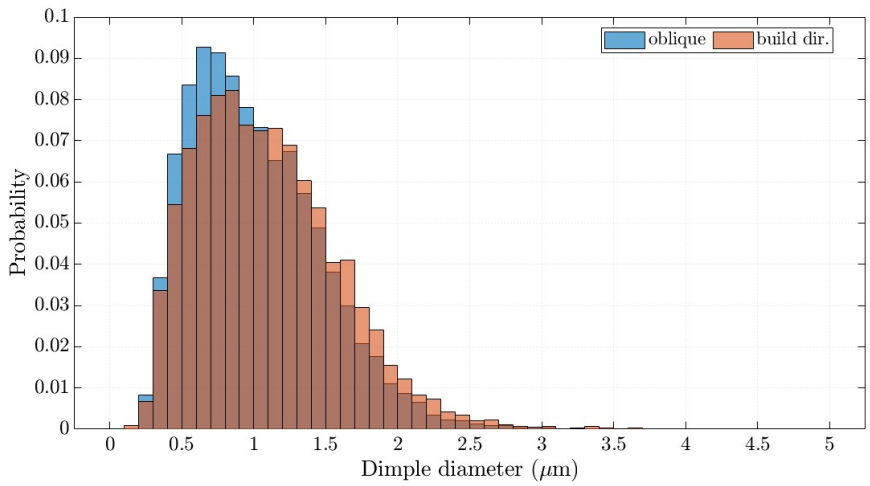

Figure 13: Distribution of the equivalent diameter of the dimple structures.

[27, 28], a structural effect is also expected as inter-layers correspond to the valleys in the thickness profile (thinnest regions). In addition, strain localization is clearly affected by the lack-of-fusion defects, which tend to concentrate strain around them.

As shown in figure 14 (c), void nucleation is also detected in the SEM micrographs at different loading stages. Void nucleation arises near the lack-of-fusion defects, and are likely responsible for strain localization. In addition, voids nucleate before the crack onset, and are aligned with the maximum stress. Thus, the crack is guided by micro-cracks that can follow the line of maximum stress regardless of the microstructure and thickness profile, as the lack-of-fusion defects are isotropically distributed at the specimen surface. In addition, these micro-cracks are likely responsible for damage identified in section 4.

7. Conclusion

This paper presents an experimental study on ductile fracture mechanisms of as-printed 316L stainless steel thin-walled structures fabricated by the directed energy deposition additive manufacturing process. In-situ experiments (tensile and fracture tests) have been carried out. Microstructures have been characterized and a strong morphological texture has been observed. Thus, anisotropy was expected and three specimen directions have been considered (i.e., 0°, 45° and 90° with respect to the build direction). Global digital image correlation techniques have been used to measure strains, and the elastic-plastic behavior is inferred from the applied load. Results suggest a slightly anisotropic hardening law, which is likely due to geometrical effects arising from thickness variations resulting from the process. Indeed, a simple model based on springs and sliding frictional elements showed that an isotropic material can reproduce the apparent anisotropy if thickness variations are taken into account. For the fracture tests, a backward digital image correlation scheme has been proposed in order to deal with the crack opening. Elastic and plastic strain and stress have been obtained. The path-independent J-integral has been computed for all fracture tests and is very similar for all specimen directions. Fracture toughness has therefore been identified. Similarly, the crack path and the crack surface have been found to be very similar for

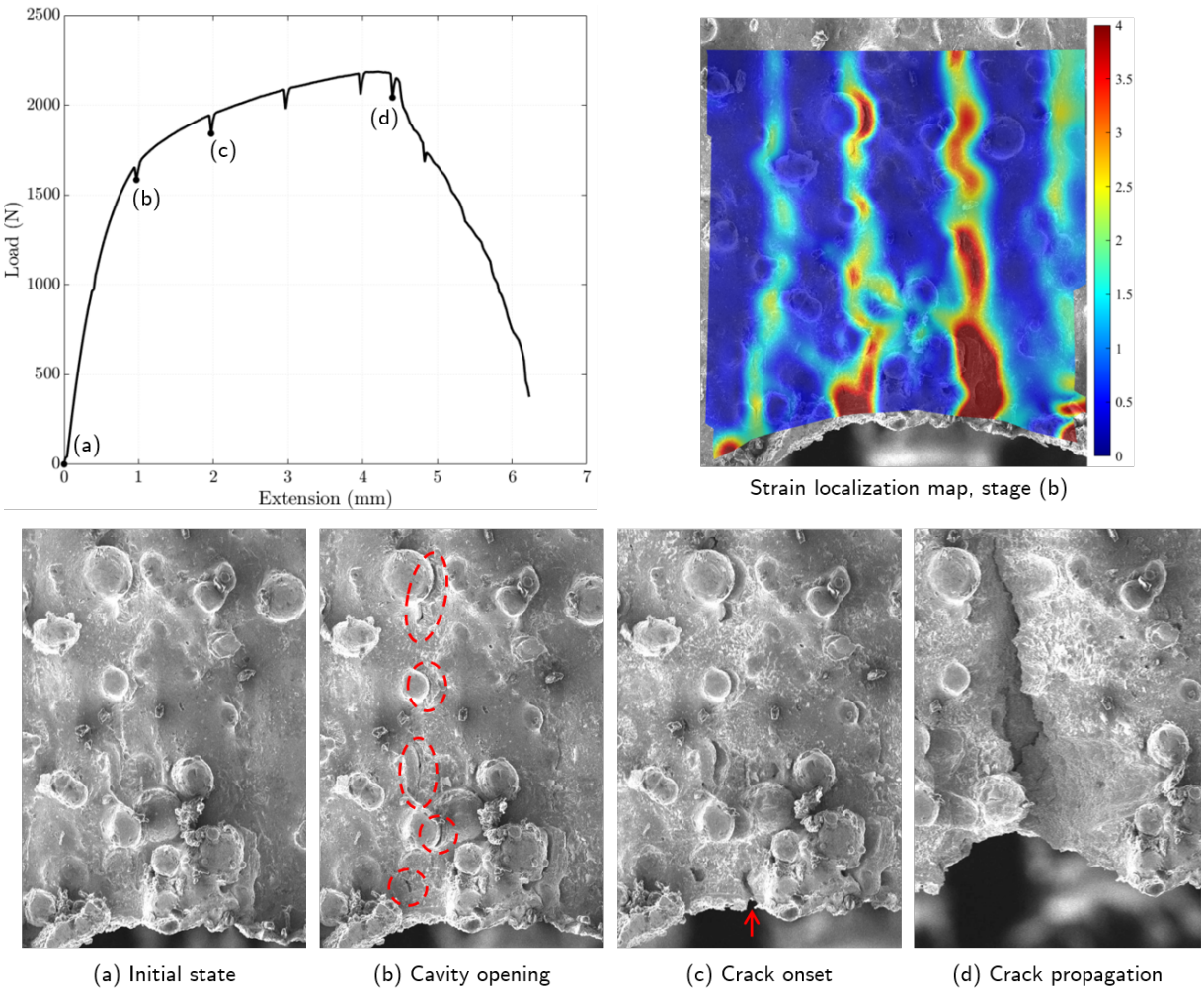

Figure 14: In-situ fracture test under a SEM. (a) Load-extension curve with labeled stages; (b) DIC equivalent strain map, normalized by the mean strain, showing strain localization; (c) SEM micrographs for the different labeled stages.

all specimens directions. To explain such isotropic fracture mechanisms, although ductile fracture involves plastic deformations, which are anisotropic, additional in-situ experiments in a scanning electron microscope have been conducted to understand, in more detail, the crack propagation mechanism. Lack-of-fusion defects have been identified to be isotropically distributed at the specimens surfaces and favor stress concentration and void nucleation, which guide the crack path along lines of maximum stress and explain the relative isotropy of fracture properties.

Acknowledgement

Part of the funding was provided by the Chaire Andre Citroen and the Direction Générale de l'Armement. The authors would like to thank Sylvain Durbecq, Alexandre Tanguy and Simon Hallais for accompanying specimen fabrication and SEM measurements. Funding from the US National Science Foundation (DMR-1710353) during the performance of some of the experiments

at the University of Texas at Austin is also acknowledged.

Appendix A. Local stress computation

In the following we describe the procedure implemented to compute local stresses from the *total* strain field $\boldsymbol{\varepsilon}$ resulting from DIC (see section 3.2).

An incompressible elastic-plastic material is considered. As a consequence, the isotropic part of the total strain vanishes (i.e $\mathrm{tr}(\boldsymbol{\varepsilon}) = 0$), it is thus fully deviatoric. The following additive decomposition into elastic and plastic strains is considered:

$$\boldsymbol{\varepsilon} = \boldsymbol{\varepsilon}^{\mathrm{e}} + \boldsymbol{\varepsilon}^{\mathrm{p}} \tag{A.1}$$

The deviatoric stress $\boldsymbol{s}$ is then related to the strains as follows:

$$\boldsymbol{s} = \boldsymbol{\sigma} - \frac{1}{3}\,\mathrm{tr}(\boldsymbol{\sigma})\,\mathbb{1} = 2\mu\,\boldsymbol{\varepsilon}^{\mathrm{e}} \tag{A.2}$$

We consider a Von-Mises flow rule with isotropic hardening. Thus, the elastic domain is defined as:

$$f(\boldsymbol{s}, p) = \Sigma_{\mathrm{eq}}(\boldsymbol{s}) - \sigma_{\mathrm{y}}(p) \leqslant 0 \quad \text{with} \quad \Sigma_{\mathrm{eq}}(\boldsymbol{s}) = \sqrt{\frac{3}{2}\,\boldsymbol{s} : \boldsymbol{s}} \quad \text{and} \quad p = \int_t \sqrt{\frac{2}{3}\,\dot{\boldsymbol{\varepsilon}}^{\mathrm{p}} : \dot{\boldsymbol{\varepsilon}}^{\mathrm{p}}}\,\mathrm{d}t \tag{A.3}$$

where Σ_{eq}, σ_{y} and p denote the equivalent stress, yield stress and cumulative plastic strain, respectively. The flow rule reads:

$$\dot{\boldsymbol{\varepsilon}}^{\mathrm{p}} = \dot{p}\,\boldsymbol{n}(\boldsymbol{s}, p) \tag{A.4}$$

where $\boldsymbol{n}(\boldsymbol{s}, p)$ denotes the outgoing normal to the elastic domain and reads:

$$\boldsymbol{n}(\boldsymbol{s}, p) = \frac{\partial f(\boldsymbol{s}, p)}{\partial \boldsymbol{s}} = \frac{3}{2}\,\frac{\boldsymbol{s}}{\sigma_{\mathrm{y}}(p)} \tag{A.5}$$

Given the i-th *known* state $\{\boldsymbol{\sigma}_i, p_i\}$ and given the total strain step $\Delta\boldsymbol{\varepsilon}$, the present procedure aims at computing the next state $\{\boldsymbol{\sigma}_{i+1}, p_{i+1}\}$. First, a *trial* stress $\boldsymbol{s}^{\mathrm{tr}}$ is computed as if the step was *purely elastic*:

$$\boldsymbol{s}^{\mathrm{tr}} = \boldsymbol{s}_i + 2\mu\,\Delta\boldsymbol{\varepsilon} \tag{A.6}$$

Hence, two cases are considered depending on the corresponding plastic criterion $f^{\mathrm{tr}} = f(\boldsymbol{s}^{\mathrm{tr}}, p_i)$:

- If $f^{\mathrm{tr}} \leqslant 0$, there is no plastic flow (i.e., $\Delta p = 0$ and $\Delta\boldsymbol{\varepsilon}^{\mathrm{p}} = 0$).
- If $f^{\mathrm{tr}} > 0$, a plastic correction is needed.

If plastic correction is needed, Δp is computed so that the deviatoric stress $\boldsymbol{s}_{i+1} = \boldsymbol{s}^{\mathrm{tr}} - 2\mu\,\Delta p\,\boldsymbol{n}$ verifies (A.3), hence:

$$\begin{aligned} f(\boldsymbol{s}_{i+1}, p_{i+1}) &= f(\boldsymbol{s}^{\mathrm{tr}} - 2\mu\,\Delta p\,\boldsymbol{n}, p_i + \Delta p) \\ &= \Sigma_{\mathrm{eq}}(\boldsymbol{s}^{\mathrm{tr}}) - 2\mu\,\Delta p - \sigma_{\mathrm{y}}(p_i + \Delta p) \\ &= 0 \end{aligned} \tag{A.7}$$

In general this last equation (A.7)is solved by an iterative Newton-Raphson procedure, which evaluates the new deviatoric stress $\boldsymbol{s}_{i+1}$ and cumulative plastic strain p_{i+1}.

However, since the material is assumed to be incompressible, the isotropic part of the stress tensor $\boldsymbol{\sigma}_{i+1}$ is not determined from the behavior. As a consequence, the stress tensor is known up to a constant c so that:

$$\boldsymbol{\sigma}_{i+1} = \boldsymbol{s}_{i+1} - c\,\mathbb{1} \tag{A.8}$$

Boundary conditions are used to identify c. Indeed the plane stress assumption gives:

$$\sigma_{33,i+1} = s_{33,i+1} - c = 0 \tag{A.9}$$

Hence, the stress tensor reads:

$$\boldsymbol{\sigma}_{i+1} = \boldsymbol{s}_{i+1} - s_{33,i+1}\,\mathbb{1} = 2\mu\left(\boldsymbol{\varepsilon}^{\mathrm{e}}_{i+1} - \varepsilon^{\mathrm{e}}_{33,i+1}\,\mathbb{1}\right) \tag{A.10}$$

Appendix B. Stress field correction

Due to measurement uncertainties (noise in DIC and imperfectly known behavior), the procedure presented in Appendix A lead to stress fields that do not verify the equilibrium equation (4). A stress correction is proposed to verify the equilibrium equation. Of course the yield stress may be slightly exceeded as stresses are modified, but this is not a significant issue as the constitutive law is imperfectly known although the equilibrium is a state equation that should be verified exactly.

The proposed correction consists of finding a deviatoric elastic strain $\boldsymbol{\varepsilon}^C$ (where the superscript C stands for *corrected*) as close as possible to the previously computed elastic strain $\boldsymbol{\varepsilon}^{\mathrm{e}}$ (as detailed in section Appendix A), and so that the resulting stresses $\boldsymbol{\sigma}^C = 2\mu\left(\boldsymbol{\varepsilon}^C - \varepsilon^C_{33}\,\mathbb{1}\right)$ verifies the equilibrium equation (4). This can be written as constrained minimization:

$$\begin{cases} \boldsymbol{\varepsilon}^C = \underset{\boldsymbol{\varepsilon}^C_*}{\operatorname{argmin}} \left[\left(\boldsymbol{\varepsilon}^C_* - \boldsymbol{\varepsilon}^{\mathrm{e}}\right) : \left(\boldsymbol{\varepsilon}^C_* - \boldsymbol{\varepsilon}^{\mathrm{e}}\right)\right] \\ \text{constraint } \mathbf{div}\left[2\mu\left(\boldsymbol{\varepsilon}^C - \varepsilon^C_{33}\mathbb{1}\right)\right] = 0 \end{cases} \tag{B.1}$$

This constrained minimization problem leads to consider the following Lagrangian:

$$\mathcal{L}(\boldsymbol{\varepsilon}^C, \boldsymbol{\lambda}) = \frac{1}{2}\int_\Omega \left(\boldsymbol{\varepsilon}^C - \boldsymbol{\varepsilon}^{\mathrm{e}}\right) : \left(\boldsymbol{\varepsilon}^C - \boldsymbol{\varepsilon}^{\mathrm{e}}\right)\,\mathrm{d}\boldsymbol{x} + \int_\Omega \boldsymbol{\lambda}\cdot\mathbf{div}\left(\boldsymbol{\varepsilon}^C - \varepsilon^C_{33}\,\mathbb{1}\right)\,\mathrm{d}\boldsymbol{x} \tag{B.2}$$

where $\boldsymbol{\lambda}(\boldsymbol{x})$ is the Lagrange multiplier field associated to the constraint. Taking the derivative of $\mathcal{L}$ with respect to $\boldsymbol{\varepsilon}$ leads to the *local* formulation of the corresponding Lagrangian minimization problem; for any trial deviatoric tensor field $\boldsymbol{\varepsilon}^*(\boldsymbol{x})$:

$$\int_\Omega \left[\left(\boldsymbol{\varepsilon}^C - \boldsymbol{\varepsilon}^{\mathrm{e}}\right) : \boldsymbol{\varepsilon}^* + \boldsymbol{\lambda}\cdot\mathbf{div}\left(\boldsymbol{\varepsilon}^* - \varepsilon^*_{33}\,\mathbb{1}\right)\right]\,\mathrm{d}\boldsymbol{x} = 0 \tag{B.3}$$

which, with the help of the divergence theorem, is rewritten as a variational formulation:

$$\int_\Omega \left[\left(\boldsymbol{\varepsilon}^C - \boldsymbol{\varepsilon}^{\mathrm{e}}\right) : \boldsymbol{\varepsilon}^* - \boldsymbol{\nabla}\boldsymbol{\lambda} : \left(\boldsymbol{\varepsilon}^* - \varepsilon^*_{33}\,\mathbb{1}\right)\right]\,\mathrm{d}\boldsymbol{x} + \int_{\partial\Omega} \boldsymbol{\lambda}\cdot\left(\boldsymbol{\varepsilon}^* - \varepsilon^*_{33}\,\mathbb{1}\right)\cdot\boldsymbol{n}\,\mathrm{d}\omega = 0 \tag{B.4}$$

where $\partial/\partial x_3 = 0$. Choosing trial fields $\boldsymbol{\varepsilon}^*$ with non-vanishing values on the boundary $\partial\Omega$ only, the boundary conditions for $\boldsymbol{\lambda}$ are obtained:

$$\forall \boldsymbol{x} \in \partial\Omega \; : \quad \boldsymbol{\lambda}(\boldsymbol{x}) = \mathbf{0} \tag{B.5}$$

Next, the equality $\boldsymbol{\nabla}\boldsymbol{\lambda} : (\boldsymbol{\varepsilon}^* - \varepsilon^*_{33}\mathbb{1}) = (\boldsymbol{\nabla}\boldsymbol{\lambda} - \mathrm{div}\boldsymbol{\lambda}\,\boldsymbol{e}_3 \otimes \boldsymbol{e}_3) : \boldsymbol{\varepsilon}^*$ is used to rewrite the domain integral (B.4). Thus, it can be shown that there exists (α, β) such as:

$$\boldsymbol{\varepsilon}^C - \boldsymbol{\varepsilon}^{\mathrm{e}} - \boldsymbol{\nabla}\boldsymbol{\lambda} + \mathrm{div}\boldsymbol{\lambda}\,\boldsymbol{e}_3 \otimes \boldsymbol{e}_3 = \alpha\mathbb{1} + \beta(\boldsymbol{e}_1 \otimes \boldsymbol{e}_2 - \boldsymbol{e}_2 \otimes \boldsymbol{e}_1) \tag{B.6}$$

Taking the symmetrical part of this last equation gives:

$$\boldsymbol{\varepsilon}^C = \boldsymbol{\varepsilon}^{\mathrm{e}} + \frac{1}{2}\left(\boldsymbol{\nabla}\boldsymbol{\lambda} + {}^{\top}\boldsymbol{\nabla}\boldsymbol{\lambda}\right) - \mathrm{div}\boldsymbol{\lambda}\,\boldsymbol{e}_3 \otimes \boldsymbol{e}_3 \tag{B.7}$$

which, can be rewritten under the following form:

$$[\boldsymbol{x} \in \Omega] \qquad \boldsymbol{\Delta}\boldsymbol{\lambda} + 3\,\mathbf{div}\,(\boldsymbol{\nabla}\boldsymbol{\lambda}) = -2\,\mathbf{div}\,(\boldsymbol{\varepsilon}^{\mathrm{e}} - \varepsilon^{\mathrm{e}}_{33}\mathbb{1}) \tag{B.8}$$

$$[\boldsymbol{x} \in \partial\Omega] \qquad \boldsymbol{\lambda} = \mathbf{0} \tag{B.9}$$

Thus, the correction procedure takes the form of a linear boundary value problem in the Lagrange multiplier field $\boldsymbol{\lambda}$ that has to be solved over the domain. Let us notice that the right side term of (B.8) would vanish if the initial estimation of stresses were verifying the equilibrium equation.

As a FE mesh is already defined in the DIC procedure, it is more convenient to express the problem in a weak form. For any virtual vector field $\boldsymbol{\lambda}^*(\boldsymbol{x})$ such that $\forall \boldsymbol{x} \in \partial\Omega$, $\boldsymbol{\lambda}^*(\boldsymbol{x}) = \mathbf{0}$, we rewrite (B.8) as:

$$\int_{\Omega} \boldsymbol{\nabla}\boldsymbol{\lambda}^* : \left[\boldsymbol{\nabla}\boldsymbol{\lambda} + 3\,{}^{\top}\boldsymbol{\nabla}\boldsymbol{\lambda}\right] \mathrm{d}\boldsymbol{x} = -2\int_{\Omega} \boldsymbol{\nabla}\boldsymbol{\lambda}^* : (\boldsymbol{\varepsilon}^{\mathrm{e}} - \varepsilon^{\mathrm{e}}_{33}\mathbb{1})\,\mathrm{d}\boldsymbol{x} \tag{B.10}$$

As it contains only first-order derivatives, this formulation can be solved by the chosen $P1$ simplex finite element mesh used in this work. The corrected elastic field $\boldsymbol{\varepsilon}^C$ is retrieved from (B.7) and the corrected stresses can be deduced.

Appendix C. Geometrical effect

In this section we propose a simple spring analogy with sliding elements disposed in series for the build direction and in parallel for the print direction (see figures C.15a and C.15b). Springs represent a discretization of the specimen. Since the thickness is not uniform, each spring has a different stiffness that is proportional to its thickness. Springs are indexed by i and their respective thicknesses are denoted by h_i, which is a discretization of $h(z)$ given in (1). Since a pure monotone tensile test is performed, the cumulative plastic strain p is identical to the plastic strain ε^{p}. An incremental procedure is proposed to deal with non-linearity. Thus, for each spring i there are several loading increments indexed by k. Calculation is done under infinitesimal strain assumption, and nominal stress and strain are computed.

(a) Springs in series (build direction).

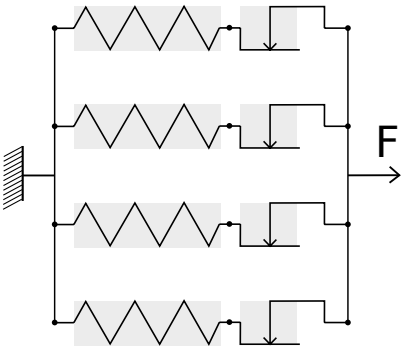

(b) Springs in parallel (print direction).

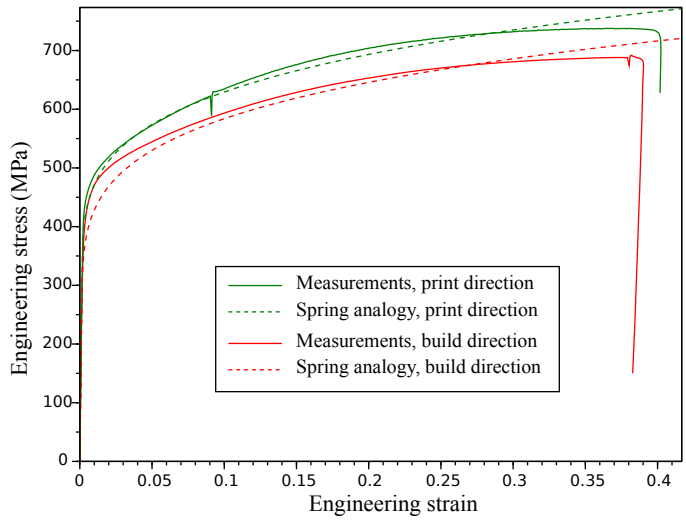

(c) Comparison between the tensile tests and the simple models with spring analogy.

Figure C.15: Spring analogy with sliding elements and comparison with tensile tests.

For springs in series, a resultant force increment per unit width ΔF is applied. Thus, the total force per unit width reads $F_k = F_{k-1} + \Delta F$. The stress increment $\Delta\sigma_{i,k}$ in the i-th spring reads:

$$\Delta\sigma_i = \frac{\Delta F}{h_i} \tag{C.1}$$

First, a *trial* stress $\sigma^{\text{tr}}_{i,k}$ is computed as if the step was *purely elastic*:

$$\sigma^{\text{tr}}_{i,k} = \sigma_{i,k-1} + \Delta\sigma_i \tag{C.2}$$

Hence, two cases are considered:

- If $\sigma^{\text{tr}}_{i,k} \leqslant \sigma_{\text{y}}(p_{i,k-1})$, there is no plastic flow, that is to say: $\Delta p_i = 0$, $\varepsilon^{\text{e}}_{i,k} = \sigma^{\text{tr}}_{i,k}/E$ and $\sigma_{i,k} = \sigma^{\text{tr}}_{i,k}$.
- If $\sigma^{\text{tr}}_{i,k} > \sigma_{\text{y}}(p_{i,k-1})$, a plastic flow should be computed.

In the second case, the flow rule gives:

$$\Delta p_i = \frac{\Delta\sigma_i}{\sigma'_{\text{y}}(p_{i,k-1})} \tag{C.3}$$

where $\sigma'_{\text{y}}(p)$ is the derivative of $\sigma_{\text{y}}(p)$ with respect to p. Thus, elastic and plastic strains are obtained

as well as the stress:

$$\begin{cases} \varepsilon^{\mathrm{p}}_{i,k} = p_{i,k} = p_{i,k-1} + \Delta p_i \\ \varepsilon^{\mathrm{e}}_{i,k} = \sigma_{\mathrm{y}}(p_{i,k})/E \\ \varepsilon_{i,k} = \varepsilon^{\mathrm{e}}_{i,k} + \varepsilon^{\mathrm{p}}_{i,k} \\ \sigma_{i,k} = \sigma_{\mathrm{y}}(p_{i,k}) \end{cases} \tag{C.4}$$

The strain in each spring $\varepsilon_{i,k}$ is a discretization of a continuous strain $\varepsilon(z,k)$. Thus, the total strain ε_k of all the springs reads:

$$\varepsilon_k = \frac{1}{\Delta z}\int_0^{\Delta z} \varepsilon(z,k)\,\mathrm{d}z \tag{C.5}$$

For springs in parallel, stress and strain are the same in all the springs. A strain increment $\Delta\varepsilon$ is applied. Thus the total strain reads $\varepsilon_k = \varepsilon_{k-1} + \Delta\varepsilon$. First, a *trial* stress σ^{tr}_k is computed as if the step was *purely elastic*:

$$\sigma^{\mathrm{th}}_k = \sigma_{k-1} + E\Delta\varepsilon \tag{C.6}$$

Hence, two cases are considered:

- If $\sigma^{\mathrm{tr}}_k \leqslant \sigma_{\mathrm{y}}(p_{k-1})$, there is no plastic flow, that is to say: $\Delta p = 0$, $\varepsilon^{\mathrm{e}}_k = \sigma^{\mathrm{tr}}_k/E$ and $\sigma_k = \sigma^{\mathrm{tr}}_k$.
- If $\sigma^{\mathrm{tr}}_k > \sigma_{\mathrm{y}}(p_{k-1})$, a plastic flow should be computed.

In the second case, the flow rule gives, with $\Delta\sigma_k = E\Delta\varepsilon^{\mathrm{e}} = E(\Delta\varepsilon - \Delta p)$:

$$\Delta p = \frac{E(\Delta\varepsilon - \Delta p)}{\sigma'_{\mathrm{y}}(p_{k-1})} \Rightarrow \Delta p = \frac{E\Delta\varepsilon}{E + \sigma'_{\mathrm{y}}(p_{k-1})} \tag{C.7}$$

Thus elastic and plastic strains are obtained as well as stresses similar to (C.4).

A single behavior is used to generate stress-strain curves for both the build direction (springs in series) and the print direction (springs in parallel). A comparison between tensile tests (build and print directions) and the corresponding computations using the spring analogy is shown in figure 7, and reasonable agreement is observed. This comparison is not meant to identify the behavior precisely, but only aims at showing that a single behavior can explain the anisotropic behavior only by considering thickness variations.

Appendix D. Dimple size measurement

The dimple size measurement results presented in Sec. 6.1 are extracted by means of image processing of the obtained SEM micrographs. The image segmentation procedure consists of the following steps: (i) background deletion by high-pass filtering; (ii) contrast enhancement via image normalization; (iii) noise removal thanks to median filtering; (iv) image segmentation by application of the a *watershed* algorithm started from local gray intensity minima. The procedure is illustrated in figure D.16 on a sub-domain of an acquired SEM micrograph.

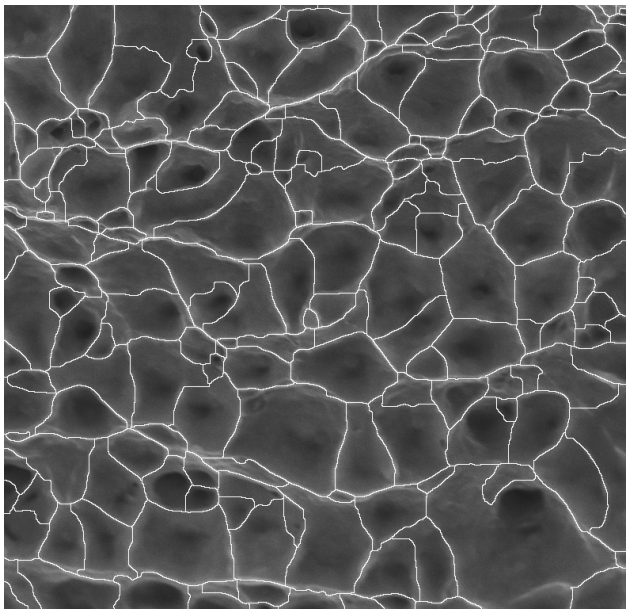

Figure D.16: Image segmentation procedure. Background: SEM micrograph; white lines: dimple boundaries.

References

[1] N. Guo, M. C. Leu, Additive manufacturing: Technology, applications and research needs, 2013.

[2] ISO/ASTM 52900: Additive manufacturing - General principles - Terminology, Technical Report, International Organization for Standardization, 2015.

[3] T. Hwang, Y. Y. Woo, S. W. Han, Y. H. Moon, Functionally graded properties in directed-energy-deposition titanium parts, Optics and Laser Technology 105 (2018) 80–88.

[4] J. M. Wilson, C. Piya, Y. C. Shin, F. Zhao, K. Ramani, Remanufacturing of turbine blades by laser direct deposition with its energy and environmental impact analysis, Journal of Cleaner Production 80 (2014) 170–178.

[5] W. E. Frazier, Metal additive manufacturing: a review, Journal of Materials Engineering and Performance 23 (2014) 1917–1928.

[6] T. DebRoy, H. Wei, J. Zuback, T. Mukherjee, J. Elmer, J. Milewski, A. M. Beese, A. Wilson-Heid, A. De, W. Zhang, Additive manufacturing of metallic components–process, structure and properties, Progress in Materials Science 92 (2018) 112–224.

[7] J. Jiang, X. Xu, J. Stringer, Support structures for additive manufacturing: a review, Journal of Manufacturing and Materials Processing 2 (2018) 64.

[8] E. R. Denlinger, J. C. Heigel, P. Michaleris, T. Palmer, Effect of inter-layer dwell time on distortion and residual stress in additive manufacturing of titanium and nickel alloys, Journal of Materials Processing Technology 215 (2015) 123–131.

[9] E. R. Denlinger, P. Michaleris, Effect of stress relaxation on distortion in additive manufacturing process modeling, Additive Manufacturing 12 (2016) 51–59.

[10] Z. Wang, T. A. Palmer, A. M. Beese, Effect of processing parameters on microstructure and tensile properties of austenitic stainless steel 304l made by directed energy deposition additive manufacturing, Acta Materialia 110 (2016) 226–235.

[11] B. A. Szost, S. Terzi, F. Martina, D. Boisselier, A. Prytuliak, T. Pirling, M. Hofmann, D. J. Jarvis, A comparative study of additive manufacturing techniques: Residual stress and microstructural analysis of clad and waam printed ti–6al–4v components, Materials & Design 89 (2016) 559–567.

[12] M. Biegler, B. Graf, M. Rethmeier, In-situ distortions in lmd additive manufacturing walls can be measured

with digital image correlation and predicted using numerical simulations, Additive Manufacturing 20 (2018) 101–110.
[13] X. Lu, X. Lin, M. Chiumenti, M. Cervera, Y. Hu, X. Ji, L. Ma, H. Yang, W. Huang, Residual stress and distortion of rectangular and s-shaped ti-6al-4v parts by directed energy deposition: modelling and experimental calibration, Additive Manufacturing 26 (2019) 166–179.
[14] Y. Kok, X. Tan, P. Wang, M. Nai, N. Loh, E. Liu, S. Tor, Anisotropy and heterogeneity of microstructure and mechanical properties in metal additive manufacturing: A critical review, Materials & Design 139 (2018) 565–586.
[15] F. M. Sciammarella, B. Salehi Najafabadi, Processing parameter doe for 316l using directed energy deposition, Journal of Manufacturing and Materials Processing 2 (2018).
[16] Y. Balit, E. Charkaluk, A. Constantinescu, Digital image correlation for microstructural analysis of deformation pattern in additively manufactured 316L thin walls, Additive Manufacturing 31 (2020) 100862.
[17] J. Pegues, M. Roach, R. Scott Williamson, N. Shamsaei, Surface roughness effects on the fatigue strength of additively manufactured Ti-6Al-4V, International Journal of Fatigue 116 (2018) 543–552.
[18] J. Robinson, I. Ashton, P. Fox, E. Jones, C. Sutcliffe, Determination of the effect of scan strategy on residual stress in laser powder bed fusion additive manufacturing, Additive Manufacturing 23 (2018) 13–24.
[19] J. Suryawanshi, K. G. Prashanth, U. Ramamurty, Mechanical behavior of selective laser melted 316L stainless steel, Materials Science and Engineering A 696 (2017) 113–121.
[20] R. Shrestha, J. Simsiriwong, N. Shamsaei, Fatigue behavior of additive manufactured 316L stainless steel parts: Effects of layer orientation and surface roughness, Additive Manufacturing 28 (2019) 23–38.
[21] Y. Balit, L.-R. Joly, F. Szmytka, S. Durbecq, E. Charkaluk, A. Constantinescu, Self-heating behavior during cyclic loadings of 316l stainless steel specimens manufactured or repaired by directed energy deposition, Materials Science and Engineering: A 786 (2020) 139476.
[22] B. Zheng, J. Haley, N. Yang, J. Yee, K. Terrassa, Y. Zhou, E. Lavernia, J. Schoenung, On the evolution of microstructure and defect control in 316l ss components fabricated via directed energy deposition, Materials Science and Engineering: A 764 (2019) 138243.
[23] D.-K. Kim, W. Woo, E.-Y. Kim, S.-H. Choi, Microstructure and mechanical characteristics of multi-layered materials composed of 316l stainless steel and ferritic steel produced by direct energy deposition, Journal of Alloys and Compounds 774 (2019) 896 – 907.
[24] Z. E. Tan, J. H. L. Pang, J. Kaminski, H. Pepin, Characterisation of porosity, density, and microstructure of directed energy deposited stainless steel aisi 316l, Additive Manufacturing 25 (2019) 286 – 296.
[25] D. Feenstra, V. Cruz, X. Gao, A. Molotnikov, N. Birbilis, Effect of build height on the properties of large format stainless steel 316l fabricated via directed energy deposition, Additive Manufacturing 34 (2020) 101205.
[26] A. Saboori, G. Piscopo, M. Lai, A. Salmi, S. Biamino, An investigation on the effect of deposition pattern on the microstructure, mechanical properties and residual stress of 316l produced by directed energy deposition, Materials Science and Engineering: A 780 (2020) 139179.
[27] Y. Balit, C. Guévenoux, A. Tanguy, M. V. Upadhyay, E. Charkaluk, A. Constantinescu, High resolution digital image correlation for microstructural strain analysis of a stainless steel repaired by directed energy deposition, Materials Letters 270 (2020) 127632.
[28] C. Guévenoux, S. Hallais, Y. Balit, A. Charles, E. Charkaluk, A. Constantinescu, Plastic strain localization induced by microstructural gradient in laser cladding repaired structures, Theoretical and Applied Fracture Mechanics 107 (2020) 102520.
[29] M. Seifi, A. Salem, D. Satko, J. Shaffer, J. J. Lewandowski, Defect distribution and microstructure heterogeneity effects on fracture resistance and fatigue behavior of ebm ti–6al–4v, International Journal of Fatigue 94 (2017) 263–287.
[30] F. Hild, S. Roux, Comparison of Local and Global Approaches to Digital Image Correlation, Experimental Mechanics 52 (2012) 1503–1519.
[31] J. Réthoré, F. Hild, S. Roux, Extended digital image correlation with crack shape optimization, International Journal for Numerical Methods in Engineering 73 (2008) 248–272.
[32] J. R. Rice, Mathematical analysis in the mechanics of fracture, Fracture: an advanced treatise 2 (1968) 191–311.
[33] J. Jiang, F. Weng, S. Gao, J. Stringer, X. Xu, P. Guo, A support interface method for easy part removal in directed

energy deposition, Manufacturing Letters 20 (2019) 30 – 33.
[34] B. Pan, H. Xie, Z. Guo, T. Hua, Full-field strain measurement using a two-dimensional Savitzky-Golay digital differentiator in digital image correlation, Optical Engineering 46 (2007) 033601.
[35] J. Passieux, R. Bouclier, Classic and inverse compositional Gauss-Newton in global DIC, International Journal for Numerical Methods in Engineering 119 (2019) 453–468.
[36] MATLAB, version 7.10.0 (R2014), The MathWorks Inc., Natick, Massachusetts, 2020.
[37] P. O. Persson, G. Strang, A simple mesh generator in MATLAB, SIAM Review 46 (2004) 329–345.
[38] J. Réthoré, A. Leygue, M. Coret, L. Stainier, E. Verron, Computational measurements of stress fields from digital images, International Journal for Numerical Methods in Engineering 113 (2018) 1810–1826.
[39] A. Leygue, R. Seghir, J. Réthoré, M. Coret, E. Verron, L. Stainier, Non-parametric material state field extraction from full field measurements, Computational Mechanics (2019) 1–9.
[40] A. Shahani, M. Rastegar, M. Botshekanan Dehkordi, H. Moayeri Kashani, Experimental and numerical investigation of thickness effect on ductile fracture toughness of steel alloy sheets, Engineering Fracture Mechanics 77 (2010) 646 – 659.
[41] D. Frómeta, S. Parareda, A. Lara, S. Molas, D. Casellas, P. Jonsén, J. Calvo, Identification of fracture toughness parameters to understand the fracture resistance of advanced high strength sheet steels, Engineering Fracture Mechanics 229 (2020) 106949.
[42] Y.-L. Kang, Z.-F. Zhang, H.-W. Wang, Q.-H. Qin, Experimental investigations of the effect of thickness on fracture toughness of metallic foils, Materials Science and Engineering: A 394 (2005) 312 – 319.
[43] U. Zerbst, M. Heinimann, C. D. Donne, D. Steglich, Fracture and damage mechanics modelling of thin-walled structures – an overview, Engineering Fracture Mechanics 76 (2009) 5 – 43.
[44] W. Qin, J. Li, Y. Liu, J. Kang, L. Zhu, D. Shu, P. Peng, D. She, D. Meng, Y. Li, Effects of grain size on tensile property and fracture morphology of 316L stainless steel, Materials Letters 254 (2019) 116–119.